remote sensing

Article

Summer Extreme Dust Activity in the Taklimakan Desert Regulated by the South Asian High

Chengyun Wang [1], Tianhe Wang [1,2,*], Ying Han [1,3], Yuanzhu Dong [1], Shanjuan He [1] and Jingyi Tang [1]

[1] Key Laboratory for Semi-Arid Climate Change of the Ministry of Education, College of Atmospheric Sciences, Lanzhou University, Lanzhou 730000, China; wangchy20@lzu.edu.cn (C.W.); hany2022@zzu.edu.cn (Y.H.); dongyzh21@lzu.edu.cn (Y.D.); heshj21@lzu.edu.cn (S.H.); tangjy19@lzu.edu.cn (J.T.)
[2] Collaborative Innovation Center for Western Ecological Safety, Lanzhou University, Lanzhou 730000, China
[3] School of Geoscience and Technology, Zhengzhou University, Zhengzhou 450001, China
* Correspondence: wangth@lzu.edu.cn

Abstract: Summer dust aerosol in the Taklimakan Desert (TD) affects not only the albedo of the snow and ice sheets on the Tibetan Plateau (TP) but also air quality and precipitation in the downstream areas. In this study, the summer extreme dust activity in the TD was jointly investigated by using satellite observations and MERRA-2 reanalysis datasets and divided into two states: dust active period and dust inactive period. The horizontal and vertical distribution of summer dust during both the dust active and inactive periods, as derived from the MERRA-2 dataset, is consistent with satellite observations. By comparing the upper-level circulation and surface meteorological elements at two periods, we identify the South Asian High (SAH) as the dominant factor driving the extreme dust activity in the TD during summer. When the SAH is centered on the Iranian Plateau (IP), the dust aerosol in the TD exhibits increased activity and is lifted to higher altitudes due to significantly enhanced westerly winds, near-surface wind speed, and an ascending motion. Conversely, when the SAH is centered on the TP, the summer dust activity shows the opposite behavior. These new findings on the regulatory mechanism of the SAH on the summer dust activity in the TD are highly significant for understanding the occurrence and transport of summer Asian dust and its potential impact on heavy precipitation in the downstream areas.

Keywords: South Asian High; Taklimakan Desert; summer dust activity

Citation: Wang, C.; Wang, T.; Han, Y.; Dong, Y.; He, S.; Tang, J. Summer Extreme Dust Activity in the Taklimakan Desert Regulated by the South Asian High. *Remote Sens.* **2023**, *15*, 2875. https://doi.org/10.3390/rs15112875

Academic Editor: Dimitris Kaskaoutis

Received: 4 May 2023
Revised: 24 May 2023
Accepted: 26 May 2023
Published: 1 June 2023

1. Introduction

Mineral dust aerosol is an important component of the atmosphere. When dust weather occurs, it not only impacts the ambient air quality [1–3] but also poses a threat to human health [4–7]. Furthermore, mineral dust aerosol can influence changes in the radiation energy budget [8,9] and atmospheric thermal structures [10], and it can be transported to the Tibetan Plateau (TP) or polar regions [11–13]. This transportation process has the potential to cause significant melting of snow and ice [14]. Additionally, mineral dust aerosol affects cloud properties through direct or indirect effects [15], which is highly significant for atmospheric circulation and regional climates. Accurately predicting dust activity is crucial for our understanding of climate change and for improving environmental quality. Therefore, studying the factors that contribute to changes in dust activity is critical for future dust predictions.

The Taklimakan Desert (TD), located in the center of the Tarim Basin and surrounded by mountains on three sides with only a narrow opening in the eastern region, is the second largest mineral dust source in the world and a significant contributor to dust emissions in Asia. During spring and summer, the TD appears to be the most frequent and steady source of dust emissions [16–20]. Due to its topography, dust aerosols in the TD are generally confined within the Tarim Basin, with most dust particles being redeposited after being lifted [21,22]. As a result, dust events in the TD are typically considered local phenomena [23]. However, under favorable weather conditions, dust aerosols from the TD can be vertically transported. When these aerosols reach sufficient height to surpass the surrounding terrain, they are carried eastward by westerlies [22,24], reaching North America across the Pacific or being transported to the Arctic under specific circulation patterns [13,25–31]. Furthermore, the TD is adjacent to the TP to the south. Dust aerosol from the TD can be transported to the plateau [32,33], influencing convective cloud formation over the TP and potentially leading to heavy rainfall in downstream areas [34]. Additionally, during summer, the dust aerosols from the TD could be trapped in the Asian Summer Monsoon Anticyclone (ASMA) under the influence of the circulation, which partly contributes to the formation of the Asian tropopause aerosol layer [35]. Therefore, understanding the main drivers of summer dust activity in the TD holds significant importance for comprehending dust transport mechanisms and regional and global climate effects.

The upper-level circulation system exhibits good stability and can reflect changes in large-scale circulation, thereby exerting a regulatory effect on the near-surface circulation field and even influencing the occurrence of dust events in the TD [36,37]. Most research has focused on the spring dust activity due to the frequent downstream transport of Asian dust during that season. It has been observed that the Westerly Jet (WJ) plays a significant role in spring dust activity. Strengthening the WJ intensifies the low-level winds in the TD, resulting in increased frequency of dust weather [38–40]. Conversely, a weakened WJ contributes to a reduction in dust events in the TP [41]. Additionally, anomalous large-scale environment conditions related to the Arctic Oscillation (AO) and El Nino-Southern Oscillation (ENSO) can create favorable conditions for the enhanced dust activities in Asia [42–45]. However, the regulation of summer dust activity in the TD by large-scale circulation has received less attention, apart from the contribution of momentum transfer of the nocturnal low-level jet [46,47].

The South Asian High (SAH), a thermal high influenced by diabatic heating over the highland and monsoon regions, is the dominant and persistent anticyclone in the upper troposphere and the lower stratosphere during boreal summer. It plays a crucial role in shaping the regional climate across Asia [48–50]. The quasi-biweekly oscillation is a seasonal characteristic of the SAH [51], leading to changes in the atmosphere's thermal structure and circulation field [52,53]. Previous studies have primarily focused on its interactions with the summer monsoon and precipitation patterns [54–59]. However, how this powerful circulation system will affect dust activity has not been clearly concluded.

In this study, the summer dust activity in the TD was classified and analyzed based on satellite observations and reanalysis datasets. Additionally, from the perspective of macroscale circulation, the effect of the SAH on TD dust activity in summer was investigated in an attempt to understand the mechanisms underlying the effect of large-scale circulation systems on summer dust activity.

2. Data and Method

2.1. Observation Data

To obtain a dust aerosol vertical distribution in the TD, the latest Version 4 Level 2 Aerosol PROfile (APRO) product of Cloud-Aerosol Lidar with Orthogonal Polarization (CALIOP) [60] for the period of 2007–2018 was used in this study. To ensure high-quality retrieval data, following Wang et al. [10] and Han et al. [24], a data-filtering scheme with Cloud-Aerosol Discrimination (CAD) score between -70 and -100 and extinction quality control flag (Ext_QC) flag values of 0, 1, 2, 16, and 18 are used. Considering the complex topography of TP, the extinction coefficient of CALIPSO was re-gridded at a resolution of 0.5° (latitude) $\times$ 1.5° (longitude).

The MODerate-resolution Imaging Spectroradiometer (MODIS), aboard the Terra and Aqua satellites, can provide global almost daily observations in 36 spectral bands of approximately 0.41–14 microns covering 2330 km. The optical properties of global aerosols can be obtained based on two complementary aerosol inversion algorithms, the "Dark

Target" algorithm (DT) and the "Deep Blue" algorithm (DB). According to the methods of Song et al. [61] and Yu et al. [62], Dust Optical Depth (DOD) over land can be extracted by using the AOD, Ångström exponent, and single-scattering albedo at 470 nm, retrieved by DB algorithm.

2.2. Reanalysis Data

The second Modern-Era Retrospective analysis for Research and Applications (MERRA-2) was generated by coupling the Goddard Earth Observation System of Systems v5 (GEOS-5) with the GOddard Chemical Aerosol Radiation and Transport (GOCART) model [63]. DOD at 550 nm was also obtained by MERRA-2, due to the assimilations of multi-source aerosol observations such as MODIS, the Multi-Angle Imaging SpectroRadiometer (MISR), and AErosol RObotic NETwork (AERONET) [64–66]. Additionally, MERRA-2 also simulates dust emission, dust mixing ratio, and deposition fluxes by using a radiatively coupled version of GOCART. All these variations have a resolution of $0.5^\circ \times 0.625^\circ$ and 72 hybrid-eta levels from the surface and to 0.01 hPa. In this study, DOD of MERRA-2 from 2000 to 2020 was used to classify dust in active and inactive periods, so as to analyze dust conditions and circulation field conditions in the two periods. The DOD distribution of MERRA-2 was verified by the DOD of MODIS, and the dust mixing ratio of MERRA-2 that was used to study the vertical distribution of dust was also used for comparison with CALIOP-based estimates. Furthermore, the 2000–2020 daily data from the National Centers for Environmental Prediction (NCEP)/Department of Energy (DOE) Reanalysis 2 (NCEP-DOE 2), on a $2.5^\circ \times 2.5^\circ$ horizontal resolution [67], were used to analyze the corresponding atmospheric circulation and surface meteorological elements.

2.3. Definition of Summer Dust Activity

To investigate the major characteristics of summer dust distribution and atmospheric circulation, all active and inactive periods of summer dust need to be delineated and then their composites computed. Here, the Summer Dust Active Period (SDAP) and Summer Dust Inactive Period (SDIP) were defined respectively for the time series of DOD from 2000 to 2020, specifically during the period from 1 June to 31 August. First, the daily DOD anomalies, averaged over the TD (77°–90°E, 35°–42°N), were estimated by subtracting the daily climatological mean. Then, these anomalies were normalized based on the corresponding standard deviation. An SDAP was identified when the normalized DOD anomalies were greater than 1.0 for at least three consecutive days during July and August. Conversely, an SDIP was identified when the normalized DOD anomalies were less than -1.0 for at least three consecutive days during the same period. In the total 1932 days of the 21 summers from 2000 to 2020, 217 days were chosen as the SDAP, and 186 days were chosen as the SDIP.

It is worth mentioning that the abnormal variables used for analysis, except for the CALIOP data, were computed using the same processing method to obtain the abnormal sequence. The abnormal variables were obtained by subtracting the corresponding daily climatological mean from each grid point, which were then presented by synthesizing corresponding SDAP/SDIP periods.

3. Results and Discussion

3.1. MERRA-2-Based Dust Activity in the TD

To examine the dust activity in each season, Figure 1a illustrates the frequency distribution of normalized DOD anomalies in different seasons within the TD region (77°–90°E, 35°–42°N) during various seasons using MERRA-2. The absolute value of the normalized DOD anomalies was greater than 1.0 and was defined as extreme dust activity. The frequency percentages of extreme dust activity in spring, summer, autumn, and winter for the period of 2000–2020 were 24.07%, 28.57%, 23.55%, and 17.30%, respectively. Notably, summer exhibited significantly higher dust activity compared with other seasons, with the greatest fluctuation in DOD anomalies observed during this period. Furthermore, the relationship between the summer dust activity in the TD and large-scale atmospheric circulation remains to be explored. Therefore, we studied the major characteristics of extreme dust activity through the example of synthetic analysis of the SDAP/SDIP to further analyze the conditions that cause summer dust activity and inactivity.

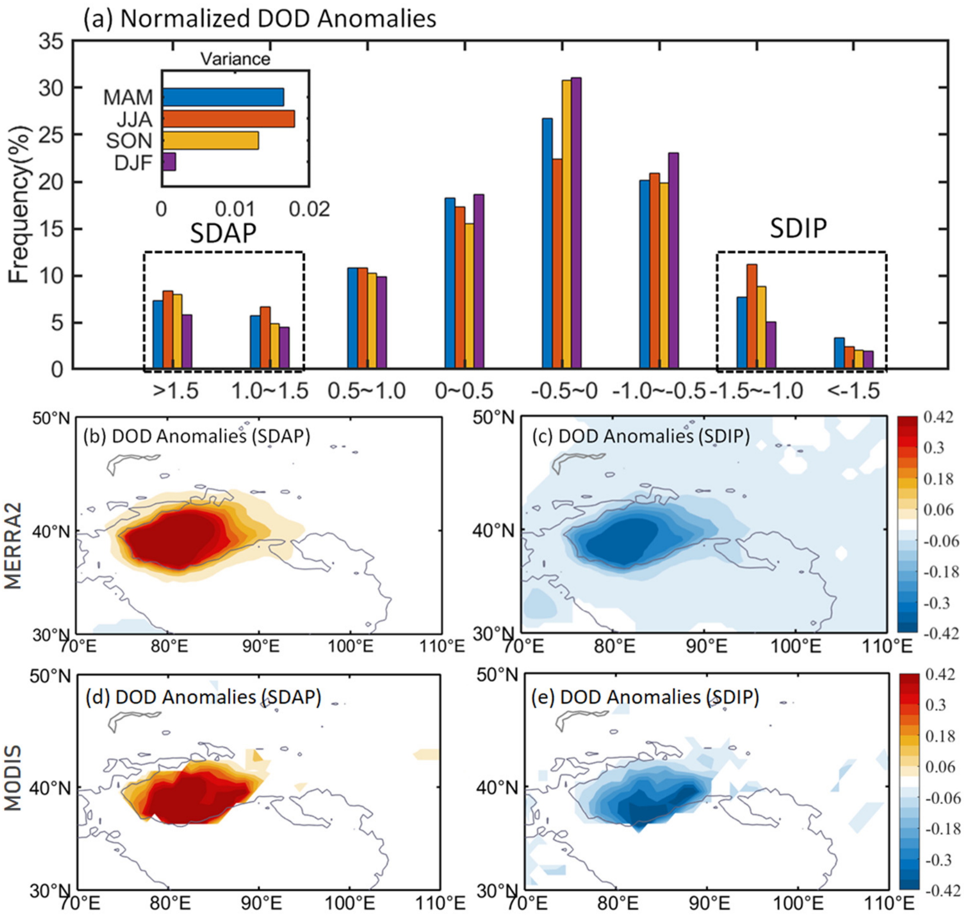

Figure 1. (**a**) Frequency of normalized Dust Optical Depth (DOD) anomaly in Taklimakan Desert (77°–90°E, 35°–42°N) from 2000 to 2020. The top left corner of the figure presents the seasonal variance of DOD anomalies for each season, with blue representing spring, orange representing summer, yellow representing autumn, and purple representing winter. (**b**–**e**) Distribution of DOD anomalies during (**b**,**d**) Summer Dust Active Period (SDAP) and (**c**,**e**) Summer Dust Inactive Period (SDIP) between 2000 and 2020, using data from MERRA-2 (upper panel) and MODIS (lower panel). The gray solid line in the figure represents the isoline at an altitude of 3000 m above sea level. The color-filled areas all passed with 95% significance.

According to the distribution of DOD anomalies in the SDAP and SDIP derived from MERRA-2 (Figure 1b,c), it is evident that dust activity is primarily concentrated in the TD region, while other dust sources do not exhibit significant DOD anomalies. In the SDAP, positive DOD anomalies are observed and concentrated in the Tarim Basin. Conversely, in the SDIP, negative DOD anomalies prevail. This observation confirms that the selected dates effectively capture the two states of extreme dust activity in the TD. The composite circulation patterns are largely responsible for the dust activity in the TD.

3.2. Satellite-Based Verification of Summer Dust Activity

We classified the extreme dust activity in the TD based on the DOD data obtained from MERRA-2, which was well verified from the DOD distribution. That was based on reanalysis data, so we also utilized DOD data from MODIS for comparison and verification (Figure 1d,e). The satellite observations align with the reanalysis results and effectively depict the dust activity. However, there is a slight disparity in the centers of the DOD anomalies. The anomaly centers in MERRA-2 are situated in the central and western regions of the basin, whereas according to MODIS data, the anomaly center is located in the central and the southeastern edge of the basin. This discrepancy may arise from the fact that the daily data of MERRA-2 were derived from averaging three-hourly data, while the daily MODIS data were based on the average of the transit data from the Terra and Aqua satellites. The composite results show that the maximum positive anomaly value of the DOD during the SDAP reaches 0.57 in MERRA-2, and the area exhibiting the largest negative DOD anomalies during the SDIP is 0.35 below the daily climatological mean state in MERRA-2. In the MODIS results, DOD anomalies reach a maximum of 0.65 and −0.48, respectively.

Furthermore, to provide a comprehensive depiction of the vertical distribution of dust, the dust mixing ratio anomaly at the zonal (average of 38°–42°N) and meridional (average of 75°–85°E) directions from MERRA-2 was compounded, as shown in Figure 2. The dust mixing ratio profile reveals that during the summer season in the TD, dust aerosols are transported vertically up to an altitude of approximately 200 hPa. Notably, there is a substantial increase in transport toward the downstream areas and the plateau, resulting in a positive anomaly in the dust layer over the plateau with a height exceeding 500 hPa during the SDAP. Conversely, during the SDIP, the transport of dust toward the downstream regions is significantly weakened. Previous studies have indicated that the dust originating from the TD region possesses the potential to be transported over long distances or southward toward the plateau under the influence of appropriate circulation patterns [25,32,68,69]. These findings emphasize that the circulation conditions during the SDAP not only have a positive impact on the dust activity within the TD region but also facilitate the transportation of dust toward the downstream areas and the plateau. In contrast, the circulation conditions during the SDIP exhibit an opposite effect.

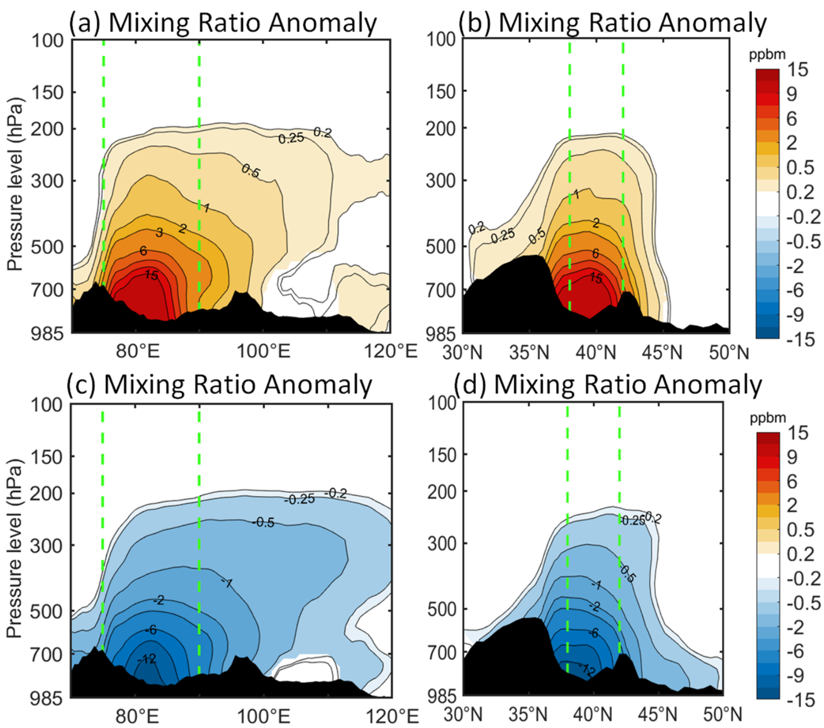

Figure 2. Composite results of the dust mixing ratio anomaly in the zonal (**left**) and meridional (**right**) directions during (**a**,**b**) SDAP and (**c**,**d**) SDIP from 2000 to 2020. The zonal distribution represents the average between 38°–42°N, while the meridional distribution corresponds to the average of 75°–85°E. The data used for these analyses were obtained from MERRA-2, and the color-filled areas in the figure indicate regions that have passed the significance threshold of 95%. The green dotted line represents the desert range (77°–90°E, 38°–42°N).

The reanalysis results of vertical distribution are given above, and consistent conclusions can be obtained from the perspective of observation. Figure 3 presents the vertical distribution of total extinction coefficient anomaly in the TD and its surroundings during the SDAP and SDIP, as captured by CALIOP. Mineral dust dominates the TD, accounting for 96% of the total aerosol extinction [70]. Therefore, the distribution of total extinction serves as a suitable indicator for characterizing the vertical dust distribution in this region. During data processing, the anomaly is calculated by subtracting the corresponding monthly average from the CALIPSO data, considering the unavailability of observed values for all grid points in the study area. Notably, a significant positive anomaly in extinction is observed during the SDAP, while the opposite is observed during the SDIP. Furthermore, the height of the extinction anomaly in the SDAP is notably greater than that in the SDIP. This suggests that dust not only exhibits higher activity during the SDAP but can also be transported to higher altitudes. When dust particles are lifted to greater heights, there is an increased likelihood of downstream transport. These findings align with the dust mixing ratio results, indicating greater transport of TD dust to downstream regions and plateaus during the SDAP.

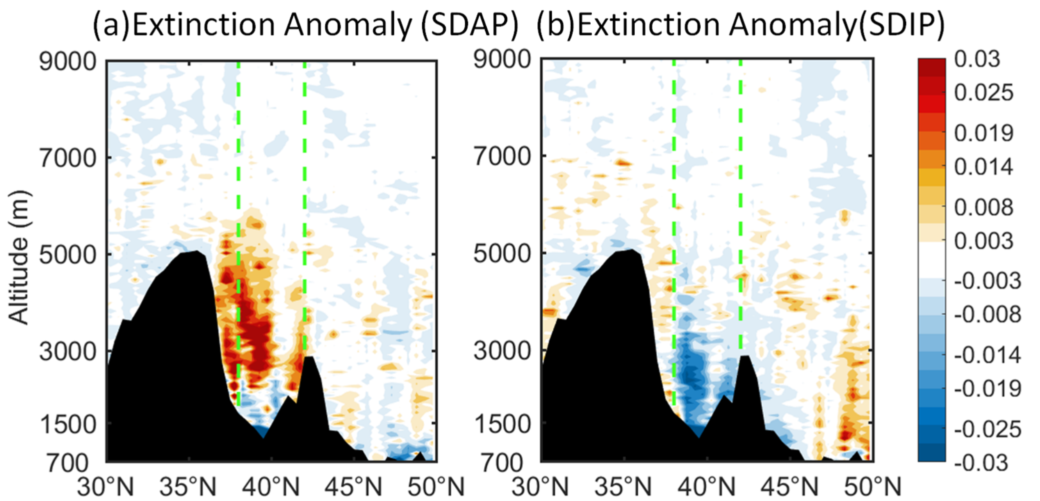

Figure 3. Composite result of meridional distribution of the total extinction coefficient anomaly from CALIOP. The analysis focuses on the average range of 75°–85°E during the (**a**) SDAP and (**b**) SDIP from 2007 to 2018.

By comparing the vertical distribution of satellite data and reanalysis data from the TD, it can be seen that positive dust-mixing ratio anomalies are observed from near the ground to high altitudes in the SDAP, whereas negative anomalies are present during the SDIP. Notably, the CALIOP data show a weak negative anomaly in aerosol extinction near the surface during the SDAP, which differs from the distribution of dust mixing ratio. This discrepancy may arise from the nature of the CALIOP data, obtained through vertically sliced scanning of the earth's atmosphere, resulting in incomplete data coverage in the study area and the inability to eliminate its annual cycle. When analyzing aerosol extinction anomalies using the CALIOP data, the monthly climate mean serves as the background field for elimination, potentially leading to larger aerosol extinction near the surface. As the MERRA-2 and CALIOP data employ different background fields for elimination, some differences in the performance of dust vertical distribution are observed. Nevertheless, the overall results indicate that aerosol extinction over the basin exceeds the monthly climate average, confirming active dust events during the SDAP.

3.3. Near-Surface Meteorological Factors

The distribution of dust emission anomalies provided by MERRA-2 is shown in Figure 4. Analysis of the 10 m actual wind field reveals a consistent northeast wind pattern in the basin during two periods of dust activity. However, the northeasterly winds during the SDAP are notably stronger than those during the SDIP. Dust emissions are largely dependent on wind patterns. The primary wind source areas in the TD are the eastern narrow entrance and the southern edge, and the highest frequency occurs in the eastern narrow entrance of the TD near Lop Nor [71]. The spatial distribution of dust emission aligns with the wind field, as the dust emission anomaly extends from the eastern entrance toward the center of the basin, with the highest anomaly value near the entrance of the Tarim basin. Correspondingly, the distribution of the dust activity anomalies also reflects the dust emission pattern, with a clear increase in dust emissions during the SDAP and a decrease during the SDIP.

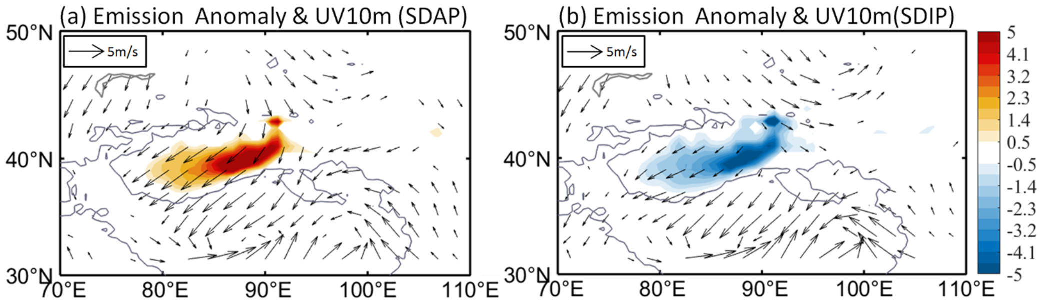

Figure 4. Composite results of dust emission anomalies (shaded) and the corresponding actual wind field at 10 m (vector) during (**a**) SDAP and (**b**) SDIP from MERRA-2 spanning 2000 to 2020. All regions depicted in the figure have undergone a 95% significance test.

Xiao, Zhou, and Liao [37] suggested that strong winds are the direct cause of dust storms in the Taklimakan region, based on site observation data. Additionally, if the surface sensible heat flux increases, the near-surface air temperature rises, which increases the near-surface turbulence and makes the air instability increase, which is conducive to the strengthening and persistence of dust weather [46,47,72,73]. In this study, we examined three primary factors influencing dust emission and investigated the differences between the SDAP and SDIP (Figure 5).

During the SDAP, the entire basin experienced abnormal northeasterly winds at the 10 m level, accompanied by positive wind speed anomalies. The SDIP exhibited opposite conditions. These differences in the wind field clearly contribute to the dust activity difference. Moreover, it was noted that the negative abnormal area of soil moisture corresponds clearly with the area of dust emission, indicating that dry soil cooperates with strong winds, making dust more active. The temperature distribution of 2 m shows that during the SDAP, the near-surface temperature is significantly higher than the daily climate average, meaning that stronger turbulence makes the blown dust mix in the air. The anomalies observed in these near-surface meteorological elements during the SDAP indicate that dust is more easily blown up from the surface and remains airborne. In contrast, the SDIP is characterized by abnormal southwest wind, evident weakening of easterly winds near the surface in the basin (Figure 2), noticeably lower near-surface temperatures than the daily climate state, and increased soil moisture. These conditions are clearly unfavorable for dust emission, defining the dust inactivity period.

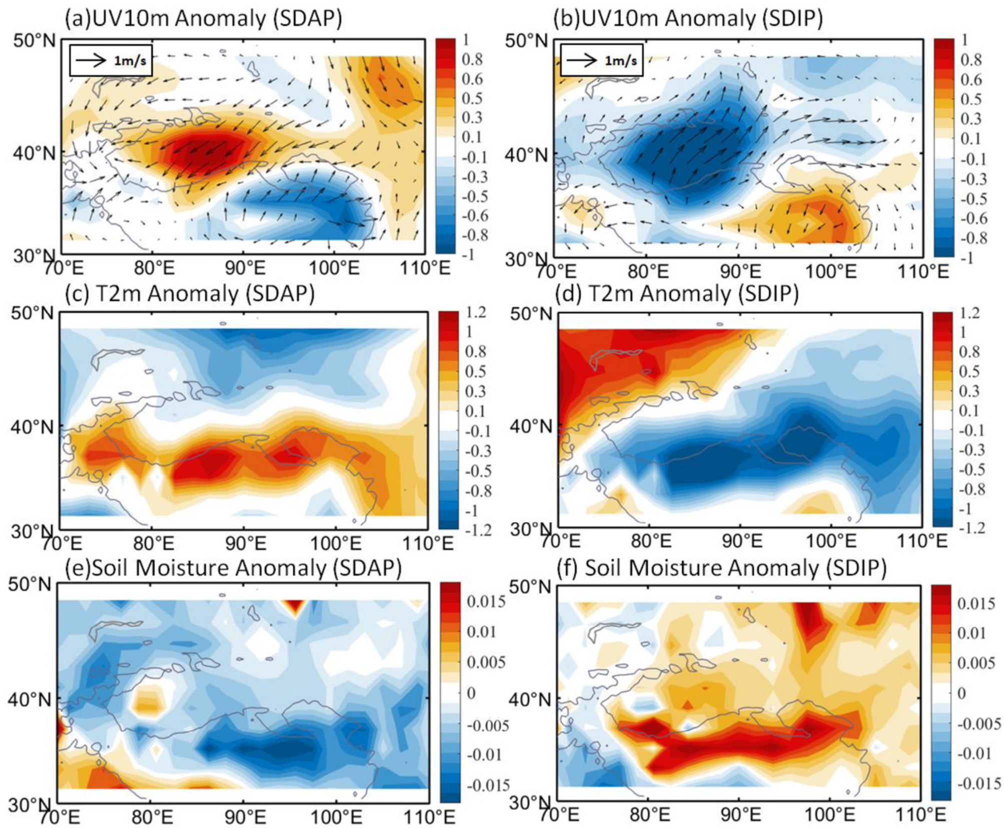

Figure 5. Composite results of (**a**) 10 m UV anomaly, (**c**) 2 m air temperature anomaly, and (**e**) soil moisture anomaly during SDAP from NCEP spanning from 2000 to 2020; correspondingly, (**b**,**d**,**f**) represent the composite results for SDIP, utilizing the same variables as (**a**–**c**), respectively.

3.4. Effect of South Asian High on Summer Dust Activity

Changes in near-surface circulation are regulated by the upper-level circulation system. To examine the role of the SAH in dust activity, the 200 hPa geopotential height, wind field, and divergence field anomalies were analyzed for the two dust active states (Figure 6). Analysis of the actual geopotential height field (contours in Figure 6) reveals that the SDAP and SDIP correspond to the western mode and eastern mode of the SAH, respectively. The geopotential height anomaly also exhibits opposite phases. During the SDAP, positive geopotential height anomalies are observed in the basin and its southwest direction. In contrast, during the SDIP, the positive geopotential height anomalies transition to negative anomalies from the basin to the Iranian Plateau (IP). The composite results of the actual geopotential height field further indicate that the SAH center during the SDAP is located near the IP, with a latitude range of 50°–80°E encompassing the 12,560 contour, while during the SDIP, the SAH center is situated near the TP, with a significantly reduced range for the 12,560 contour.

During the SDAP, the SAH assumes an IP mode, leading to the formation of an intense upper-level divergence over central Asia, centered around 42.5°N and 75°E (Figure 6c) [74]. This upper-level divergence anomaly promotes ascending motion anomalies over the basin (Figure 7a,b). As air rises from the basin, fresh air is drawn in from the entrance of the basin, thus strengthening near-surface northeasterly winds (Figure 5). Supported by the dry underlying surface, more dust particles are carried into the air, and the high near-surface temperatures enhance turbulent mixing, resulting in extreme dust events in the TD.

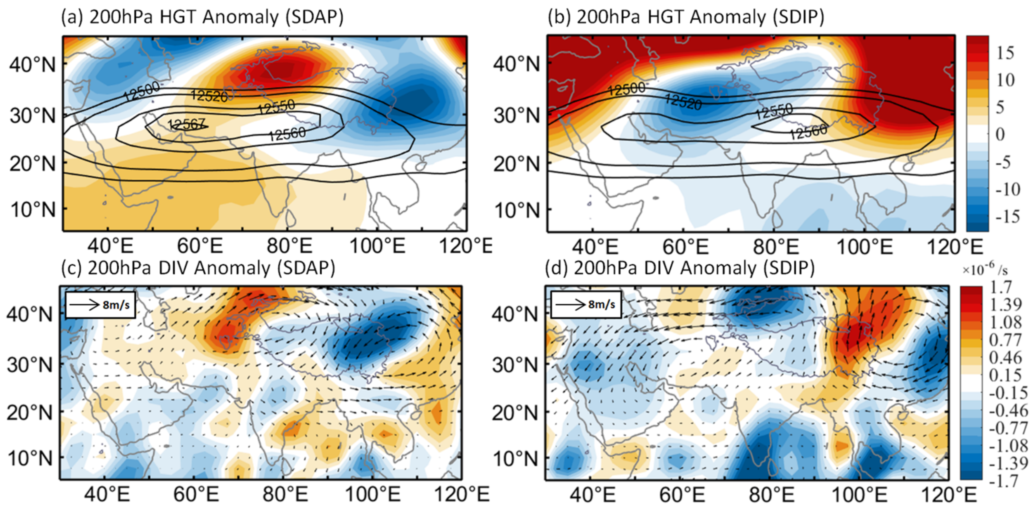

Figure 6. (**a**,**b**) Composite results of 200 hPa geopotential height (HGT) anomalies (shaded) and actual geopotential height (HGT) (contour) for the SDAP (left) and SDIP (right) from 2000 to 2020. (**c**,**d**) Composite results of 200 hPa DIVergence (DIV) anomalies (shaded) and UV anomalies (vectors) for the SDAP (**left**) and SDIP (**right**) from 2000 to 2020. The contour lines for HGT are 12,500, 12,520, 12,550, 12,560, and 12,567, from outer to inner.

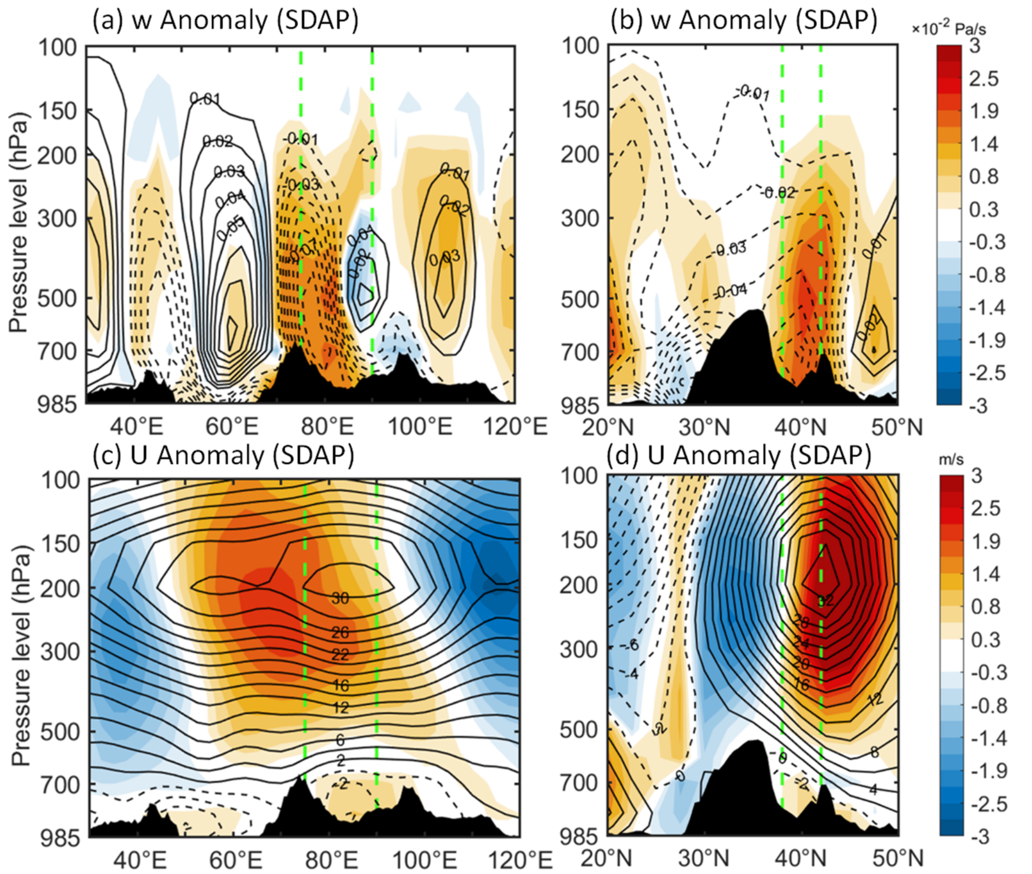

Figure 7. Composite results of zonal (**left**) and meridional (**right**) distribution of the ω anomaly (shaded in (**a**,**b**)) and the U anomaly (shaded in (**c**,**d**)) during SDAP from 2000 to 2020. The contours represent the actual ω and U fields, respectively. The zonal (meridional) distribution is averaged over the range of 38°–42°N (75°–85°E); the solid line indicates regions of downward motion or eastward motion; the green dotted line represents the desert range (77°–90°E, 38°–42°N).

In addition, a pair of cyclone–anticyclone anomalies corresponding to the SAH is observed at 200 hPa, with an abnormal anticyclone in the west and an anomalous cyclone in the east. The TD is situated at the northern edge of the abnormal anticyclone, resulting in intensified westerly winds over the basin (Figure 7c,d). The composite analysis reveals westerly winds during the SDAP exceeding 32 m/s, indicating a higher likelihood of WJ formation. Previous research by Banerjee et al. [75] has emphasized the significance of the strength and the positioning of the upper-level jet stream in influencing surface-level easterlies. Strengthened westerly winds enhance the dust's transport capacity downstream. Thus, when the SAH is in the IP mode, both the upward motion and upper-level westerly winds intensify over the basin, promoting the development of the WJ. These enhanced upward motions and westerly winds augment the dust's potential to rise to higher altitudes and facilitate its long-distance transport to the plateau or over long distances.

However, the circulation field anomaly in the SDIP exhibits a complete opposite pattern compared with the SDAP. During the SDIP, there is a negative divergence anomaly over the basin (Figure 6d), which hampers the upward motion within the basin (Figure 8). Consequently, the surface wind speed experiences a significant weakening. Additionally, the soil moisture in the SDIP is not excessively dry, which inhibits dust emission. Moreover, the basin is located on the northeast side of the anomalous cyclone, resulting in abnormal easterly winds over the TD and a weakening of the westerlies. The composite meridian distribution of U-wind shows that the center of westerlies in the SDAP is located at 42°N and 200 hPa, and it is noticeably weaker than that during the SDAP. The composite result indicates westerly winds in the SDIP of less than 28 m/s (Figure 8). Although an upward motion is still prevalent in the basin, it is evidently weakened, suggesting that the dust may not be elevated very high after being discharged. Furthermore, the upper-level westerly winds are significantly weakened, reducing their ability to transport dust eastward.

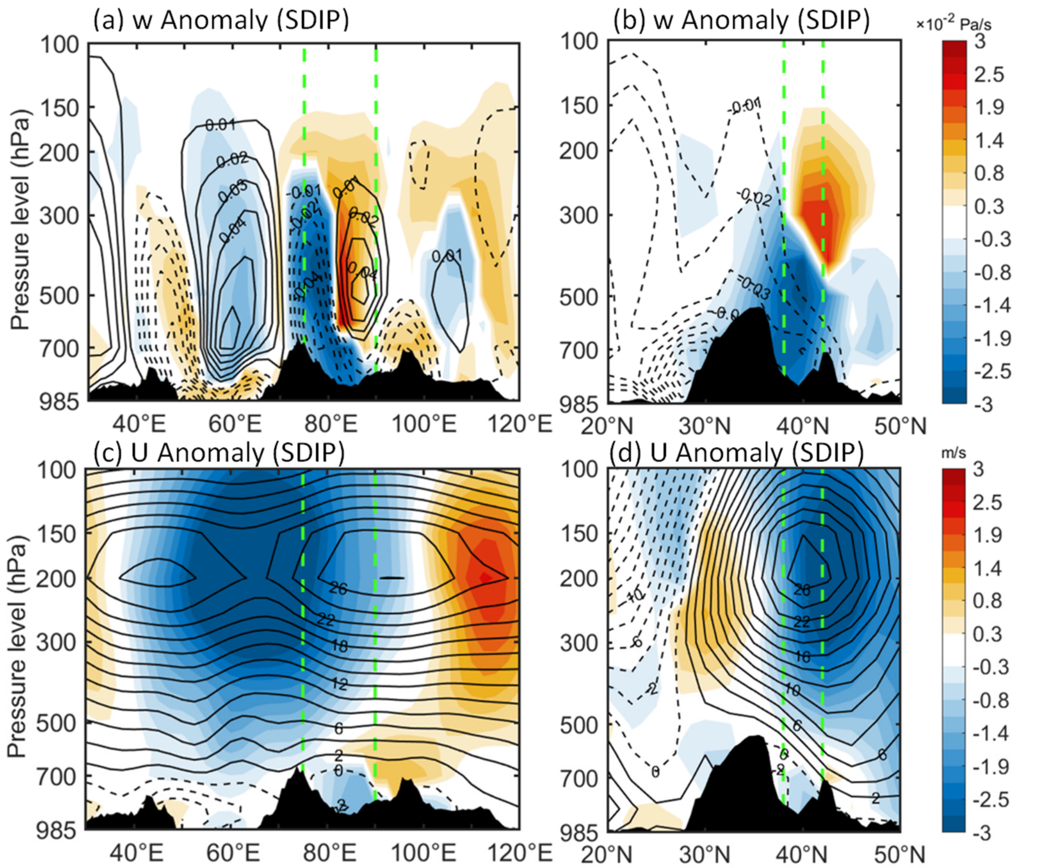

Figure 8. Same variables as in Figure 7 but for the SDIP.

4. Conclusions

The dust activity in the TD plays a crucial role in the plateau climate, as well as the air quality and precipitation in the downstream region. Summer exhibits significant variations in TD dust activity, yet the influence of large-scale circulation on summer dust activity has received limited attention. Therefore, this study focuses primarily on dust activity in summer. In this study, the dust activity in the TD during summer was divided into two states by utilizing the DOD from MERRA-2. In terms of the horizontal distribution, the DOD distribution from MERRA-2 and MODIS in these two states had a good consistency. For the vertical structure of dust, the dust mixing ratio from MERRA-2 was employed, and its authenticity was verified by comparing it with the vertical distribution of aerosol extinction from CALIOP. The extreme dust activity was defined by reanalysis data, while there was good agreement between the reanalysis and the satellite observation data in terms of the horizontal and vertical distribution of dust. This confirms the significance and reliability of the dust activity classification. The main circulation characteristics affecting dust activity can be characterized by compounding the circulation in these two states of dust activity.

By comparing the circulation patterns during two periods, the mechanism of dust events under the circulation controlled by the SAH was revealed. It was observed that the SAH, in different modes, not only directly impacts the vertical movement of the basin but also influences the strength of the west wind over the basin, thereby affecting the intensity of the WJ. When the SAH is of the western mode (with the center located over the IP), strong divergence areas form near 42.5°N and 75°E, with the basin positioned on the northern side of the anticyclones. On the one hand, the upper-level divergence induced by the SAH significantly enhances the ascending motion over the basin, regulating the intensity of low-level easterly winds. Consequently, the dust is more active during the SDAP. On the other hand, the westerly winds over the basin are strengthened by the anomalous anticyclone, which is conducive to the generation of the WJ. The amplified upper-level westerly wind enhances the transport capacity of TD dust. TD dust in the SDAP has more potential to affect the downstream area. Conversely, when the SAH is of the eastern mode (with the center located over the TP), a negative divergence anomaly emerges over the basin, resulting in a weakened ascending motion. The ability of dust to be lifted into the westerlies is reduced. More dust may be redeposited in the TD. Meanwhile, the basin is situated on the northern side of the anomalous cyclone, further diminishing the capability of upper westerly winds to transport dust downstream.

The findings of this study indicate that the SAH exerts a significant influence on dust activity in the TD. The impact of large-scale circulation patterns on the occurrence of dust events may open a pathway for us to forecast extreme dust events. The high predictability of the SAH and its regulating effect on dust activity is helpful to enhance our understanding of the influence of large circulation fields on dust activity and provides a way to improve the prediction of extreme dust events and heavy precipitation in East Asia.

Author Contributions: Conceptualization, C.W. and T.W.; methodology, C.W. and T.W.; software, C.W., Y.H. and Y.D.; validation, C.W., T.W. and Y.H.; formal analysis, C.W.; investigation, J.T., S.H. and Y.D.; resources, C.W. and T.W.; data curation, Y.H., Y.D., J.T. and S.H.; writing—original draft preparation, C.W.; writing—review and editing, T.W. and Y.H.; visualization, C.W. and S.H.; supervision, T.W. and Y.H.; project administration, T.W.; funding acquisition, T.W. All authors have read and agreed to the published version of the manuscript.

Funding: This research is jointly supported by the Second Tibetan Plateau Scientific Expedition and Research Program (STEP, 2019QZKK0602), the National Natural Science Foundation of China (42075174), and the Fundamental Research Funds for the Central Universities (lzujbky-2022-kb11).

Data Availability Statement: CALIPSO data were processed from the NASA Langley Research Center Atmospheric Science Data Center (http://eosweb.larc.nasa.gov/, accessed on 12 August 2021). MERRA-2 data were acquired from the NASA Giovanni online data system (https://giovanni.gsfc.nasa.gov/giovanni/, accessed on 12 August 2021), developed and maintained by the NASA GES DISC. The MODIS data were obtained from the NASA Goddard Earth Sciences Data and Information Services Center (GES DISC) (https://ladsweb.modaps.eosdis.nasa.gov/, accessed on 6 June 2022). NCEP-DOE Reanalysis 2 data were provided by the NOAA/OAR/ESRL PSD, Boulder, Colorado, USA (https://www.esrl.noaa.gov/psd/, accessed on 16 October 2022).

Acknowledgments: We appreciate the NASA group for making satellite datasets accessible to the public.

Conflicts of Interest: The authors declare no conflict of interest.

References

1. Park, S.H.; Gong, S.L.; Gong, W.; Makar, P.A.; Moran, M.D.; Zhang, J.; Stroud, C.A. Relative impact of windblown dust versus anthropogenic fugitive dust in PM2.5 on air quality in North America. *J. Geophys. Res.-Atmos.* **2010**, *115*, D16210. [CrossRef]
2. Kim, H.S.; Chung, Y.S.; Yoon, M.B. An analysis on the impact of large-scale transports of dust pollution on air quality in East Asia as observed in central Korea in 2014. *Air Qual. Atmos. Health* **2016**, *9*, 83–93. [CrossRef]
3. Parajuli, S.P.; Stenchikov, G.L.; Ukhov, A.; Kim, H. Dust Emission Modeling Using a New High-Resolution Dust Source Function in WRF-Chem With Implications for Air Quality. *J. Geophys. Res.-Atmos.* **2019**, *124*, 10109–10133. [CrossRef]
4. Sternberg, T.; Edwards, M. Desert Dust and Health: A Central Asian Review and Steppe Case Study. *Int. J. Environ. Res. Public Health* **2017**, *14*, 1342. [CrossRef]
5. Tobias, A.; Karanasiou, A.; Amato, F.; Roque, M.; Querol, X. Health effects of desert dust and sand storms: A systematic review and meta-analysis protocol. *BMJ Open* **2019**, *9*, e029876. [CrossRef]
6. Querol, X.; Tobias, A.; Perez, N.; Karanasiou, A.; Amato, F.; Stafoggia, M.; Garcia-Pando, C.P.; Ginoux, P.; Forastiere, F.; Gumy, S.; et al. Monitoring the impact of desert dust outbreaks for air quality for health studies. *Environ. Int.* **2019**, *130*, 104867. [CrossRef]
7. Lwin, K.S.; Tobias, A.; Chua, P.L.; Yuan, L.; Thawonmas, R.; Ith, S.; Htay, Z.W.; Yu, L.S.; Yamasaki, L.; Roque, M.; et al. Effects of Desert Dust and Sandstorms on Human Health: A Scoping Review. *Geohealth* **2023**, *7*, e2022GH000728. [CrossRef]
8. Huang, J.; Fu, Q.; Su, J.; Tang, Q.; Minnis, P.; Hu, Y.; Yi, Y.; Zhao, Q. Taklimakan dust aerosol radiative heating derived from CALIPSO observations using the Fu-Liou radiation model with CERES constraints. *Atmos. Chem. Phys.* **2009**, *9*, 4011–4021. [CrossRef]
9. Wang, T.H.; Han, Y.; Hua, W.L.; Tang, J.Y.; Huang, J.P.; Zhou, T.; Huang, Z.W.; Bi, J.R.; Xie, H.L. Profiling Dust Mass Concentration in Northwest China Using a Joint Lidar and Sun-Photometer Setting. *Remote Sens.* **2021**, *13*, 1099. [CrossRef]
10. Wang, T.H.; Han, Y.; Huang, J.P.; Sun, M.X.; Jian, B.D.; Huang, Z.W.; Yan, H.R. Climatology of Dust-Forced Radiative Heating Over the Tibetan Plateau and Its Surroundings. *J. Geophys. Res.-Atmos.* **2020**, *125*, e2020JD032942. [CrossRef]
11. Huang, J.P.; Minnis, P.; Yi, Y.H.; Tang, Q.; Wang, X.; Hu, Y.X.; Liu, Z.Y.; Ayers, K.; Trepte, C.; Winker, D. Summer dust aerosols detected from CALIPSO over the Tibetan Plateau. *Geophys. Res. Lett.* **2007**, *34*, L18805. [CrossRef]
12. Hu, Z.Y.; Huang, J.P.; Zhao, C.; Jin, Q.J.; Ma, Y.Y.; Yang, B. Modeling dust sources, transport, and radiative effects at different altitudes over the Tibetan Plateau. *Atmos. Chem. Phys.* **2020**, *20*, 1507–1529. [CrossRef]
13. Huang, Z.W.; Huang, J.P.; Hayasaka, T.; Wang, S.S.; Zhou, T.; Jin, H.C. Short-cut transport path for Asian dust directly to the Arctic: A case study. *Environ. Res. Lett.* **2015**, *10*, 114018. [CrossRef]
14. Gautam, R.; Hsu, N.C.; Lau, W.K.M.; Yasunari, T.J. Satellite observations of desert dust-induced Himalayan snow darkening. *Geophys. Res. Lett.* **2013**, *40*, 988–993. [CrossRef]
15. Yin, Y.; Chen, L. The effects of heating by transported dust layers on cloud and precipitation: A numerical study. *Atmos. Chem. Phys.* **2007**, *7*, 3497–3505. [CrossRef]
16. Zhang, X.Y.; Gong, S.L.; Zhao, T.L.; Arimoto, R.; Wang, Y.Q.; Zhou, Z.J. Sources of Asian dust and role of climate change versus desertification in Asian dust emission. *Geophys. Res. Lett.* **2003**, *30*, 2272. [CrossRef]
17. Laurent, B.; Marticorena, B.; Bergametti, G.; Chazette, P.; Maignan, F.; Schmechtig, C. Simulation of the mineral dust emission frequencies from desert areas of China and Mongolia using an aerodynamic roughness length map derived from the POLDER/ADEOS 1 surface products. *J. Geophys. Res.-Atmos.* **2005**, *110*, D18s04. [CrossRef]
18. Laurent, B.; Marticorena, B.; Bergametti, G.; Mei, F. Modeling mineral dust emissions from Chinese and Mongolian deserts. *Glob. Planet. Chang.* **2006**, *52*, 121–141. [CrossRef]
19. Shi, Z.G.; Liu, X.D. Distinguishing the provenance of fine-grained eolian dust over the Chinese Loess Plateau from a modelling perspective. *Tellus B Chem. Phys. Meteorol.* **2011**, *63*, 959–970. [CrossRef]
20. Wei, G.R.; Zhang, C.L.; Li, Q.; Wang, R.D.; Wang, H.T.; Zhang, Y.J.; Yuan, Y.X.; Li, W.P. Grain-size composition of the surface sediments in Chinese deserts and the associated dust emission. *Catena* **2022**, *219*, 106615. [CrossRef]
21. Chen, S.Y.; Huang, J.P.; Li, J.X.; Jia, R.; Jiang, N.X.; Kang, L.T.; Ma, X.J.; Xie, T.T. Comparison of dust emissions, transport, and deposition between the Taklimakan Desert and Gobi Desert from 2007 to 2011. *Sci. China Earth Sci.* **2017**, *60*, 1338–1355. [CrossRef]

22. Chen, S.Y.; Huang, J.P.; Kang, L.T.; Wang, H.; Ma, X.J.; He, Y.L.; Yuan, T.G.; Yang, B.; Huang, Z.W.; Zhang, G.L. Emission, transport, and radiative effects of mineral dust from the Taklimakan and Gobi deserts: Comparison of measurements and model results. *Atmos. Chem. Phys.* **2017**, *17*, 2401–2421. [CrossRef]
23. Liu, L.; Guo, J.P.; Gong, H.N.; Li, Z.Q.; Chen, W.; Wu, R.G.; Wang, L.; Xu, H.; Li, J.; Chen, D.D.; et al. Contrasting influence of Gobi and Taklimakan Deserts on the Dust Aerosols in Western North America. *Geophys. Res. Lett.* **2019**, *46*, 9064–9071. [CrossRef]
24. Han, Y.; Wang, T.H.; Tang, J.Y.; Wang, C.Y.; Jian, B.D.; Huang, Z.W.; Huang, J.P. New insights into the Asian dust cycle derived from CALIPSO lidar measurements. *Remote Sens. Environ.* **2022**, *272*, 112906. [CrossRef]
25. Sun, J.M.; Zhang, M.Y.; Liu, T.S. Spatial and temporal characteristics of dust storms in China and its surrounding regions, 1960–1999: Relations to source area and climate. *J. Geophys. Res.-Atmos.* **2001**, *106*, 10325–10333. [CrossRef]
26. Fang, X.M.; Han, Y.X.; Ma, J.H.; Song, L.C.; Yang, S.L.; Zhang, X.Y. Dust storms and loess accumulation on the Tibetan Plateau: A case study of dust event on 4 March 2003 in Lhasa. *Chin. Sci. Bull.* **2004**, *49*, 953–960. [CrossRef]
27. Zhang, B.; Tsunekawa, A.; Tsubo, M. Contributions of sandy lands and stony deserts to long-distance dust emission in China and Mongolia during 2000–2006. *Glob. Planet. Chang.* **2008**, *60*, 487–504. [CrossRef]
28. Yumimoto, K.; Eguchi, K.; Uno, I.; Takemura, T.; Liu, Z.; Shimizu, A.; Sugimoto, N.; Strawbridge, K. Summertime trans-Pacific transport of Asian dust. *Geophys. Res. Lett.* **2010**, *37*, L18815. [CrossRef]
29. Cao, J.H.; Chen, S.Y. The Tibetan Plateau as dust aerosol transit station in middle troposphere over northern East Asia: A case study. *Atmos. Res.* **2022**, *280*, 106416. [CrossRef]
30. Guo, J.P.; Lou, M.Y.; Miao, Y.C.; Wang, Y.; Zeng, Z.L.; Liu, H.; He, J.; Xu, H.; Wang, F.; Min, M.; et al. Trans-Pacific transport of dust aerosols from East Asia: Insights gained from multiple observations and modeling. *Environ. Pollut.* **2017**, *230*, 1030–1039. [CrossRef]
31. Yumimoto, K.; Eguchi, K.; Uno, I.; Takemura, T.; Liu, Z.; Shimizu, A.; Sugimoto, N. An elevated large-scale dust veil from the Taklimakan Desert: Intercontinental transport and three-dimensional structure as captured by CALIPSO and regional and global models. *Atmos. Chem. Phys.* **2009**, *9*, 8545–8558. [CrossRef]
32. Jia, R.; Liu, Y.Z.; Chen, B.; Zhang, Z.J.; Huang, J.P. Source and transportation of summer dust over the Tibetan Plateau. *Atmos. Environ.* **2015**, *123*, 210–219. [CrossRef]
33. Yuan, T.G.; Chen, S.Y.; Huang, J.P.; Wu, D.Y.; Lu, H.; Zhang, G.L.; Ma, X.J.; Chen, Z.Q.; Luo, Y.; Ma, X.H. Influence of Dynamic and Thermal Forcing on the Meridional Transport of Taklimakan Desert Dust in Spring and Summer. *J. Clim.* **2019**, *32*, 749–767. [CrossRef]
34. Liu, Y.Z.; Huang, J.P.; Wang, T.H.; Li, J.M.; Yan, H.R.; He, Y.L. Aerosol-cloud interactions over the Tibetan Plateau: An overview. *Earth-Sci. Rev.* **2022**, *234*, 104216. [CrossRef]
35. Tanaka, T.Y. Numerical Study of the Seasonal Variation of Elevated Dust Aerosols from the Taklimakan Desert. *Sola* **2012**, *8*, 98–102. [CrossRef]
36. Liu, Y.; Wang, G.P.; Hu, Z.Y.; Shi, P.J.; Lyu, Y.L.; Zhang, G.M.; Gu, Y.; Liu, Y.; Hong, C.; Guo, L.L.; et al. Dust storm susceptibility on different land surface types in arid and semiarid regions of northern China. *Atmos. Res.* **2020**, *243*, 105031. [CrossRef]
37. Xiao, F.J.; Zhou, C.P.; Liao, Y.M. Dust storms evolution in Taklimakan Desert and its correlation with climatic parameters. *J. Geogr. Sci.* **2008**, *18*, 415–424. [CrossRef]
38. Han, W.X.; Lu, S.; Appel, E.; Berger, A.; Madsen, D.; Vandenberghe, J.; Yu, L.P.; Han, Y.X.; Yang, Y.B.; Zhang, T.; et al. Dust Storm Outbreak in Central Asia After similar to 3.5 kyr BP. *Geophys. Res. Lett.* **2019**, *46*, 7624–7633. [CrossRef]
39. Mao, R.; Ho, C.H.; Shao, Y.P.; Gong, D.Y.; Kim, J. Influence of Arctic Oscillation on dust activity over northeast Asia. *Atmos. Environ.* **2011**, *45*, 326–337. [CrossRef]
40. Fan, K.; Wang, H.J. Interannual variability of dust weather frequency in Beijing and its global atmospheric circulation. *Chin. J. Geophys.* **2006**, *49*, 1006–1014. [CrossRef]
41. Kang, L.T.; Huang, J.P.; Chen, S.Y.; Wang, X. Long-term trends of dust events over Tibetan Plateau during 1961–2010. *Atmos. Environ.* **2016**, *125*, 188–198. [CrossRef]
42. Shi, L.M.; Zhang, J.H.; Zhang, D.; Wang, J.W.; Meng, X.L.; Liu, Y.Q.; Yao, F.M. What caused the interdecadal shift in the El Nino-Southern Oscillation (ENSO) impact on dust mass concentration over northwestern South Asia? *Atmos. Chem. Phys.* **2022**, *22*, 11255–11274. [CrossRef]
43. Li, J.; Garshick, E.; Huang, S.D.; Koutrakis, P. Impacts of El Nino-Southern Oscillation on surface dust levels across the world during 1982–2019. *Sci. Total Environ.* **2021**, *769*, 144566. [CrossRef] [PubMed]
44. Le, T.; Bae, D.H. Causal influences of El Nino-Southern Oscillation on global dust activities. *Atmos. Chem. Phys.* **2022**, *22*, 5253–5263. [CrossRef]
45. Lee, Y.G.; Kim, J.; Ho, C.H.; An, S.I.; Cho, H.K.; Mao, R.; Tian, B.J.; Wu, D.; Lee, J.N.; Kalashnikova, O.; et al. The effects of ENSO under negative AO phase on spring dust activity over northern China: An observational investigation. *Int. J. Climatol.* **2015**, *35*, 935–947. [CrossRef]
46. Ge, J.M.; Liu, H.Y.; Huang, J.P.; Fu, Q. Taklimakan Desert nocturnal low-level jet: Climatology and dust activity. *Atmos. Chem. Phys.* **2016**, *16*, 7773–7783. [CrossRef]
47. Han, Z.H.; Ge, J.M.; Chen, X.Y.; Hu, X.Y.; Yang, X.; Du, J.J. Dust Activities Induced by Nocturnal Low-Level Jet Over the Taklimakan Desert from WRF-Chem Simulation. *J. Geophys. Res.-Atmos.* **2022**, *127*, e2021JD036114. [CrossRef]

48. Zhang, P.F.; Liu, Y.M.; He, B.A. Impact of East Asian Summer Monsoon Heating on the Interannual Variation of the South Asian High. *J. Clim.* **2016**, *29*, 159–173. [CrossRef]
49. Jin, Q.; Yang, X.Q.; Sun, X.G.; Fang, J.B. East Asian summer monsoon circulation structure controlled by feedback of condensational heating. *Clim. Dyn.* **2013**, *41*, 1885–1897. [CrossRef]
50. Duan, A.M.; Wu, G.X. Role of the Tibetan Plateau thermal forcing in the summer climate patterns over subtropical Asia. *Clim. Dyn.* **2005**, *24*, 793–807. [CrossRef]
51. Liu, Y.M.; Hoskins, B.; Blackburn, M. Impact of Tibetan orography and heating on the summer flow over Asia. *J. Meteorol. Soc. Jpn.* **2007**, *85b*, 1–19. [CrossRef]
52. Ren, R.C.; Zhu, C.D.; Cai, M. Linking quasi-biweekly variability of the South Asian high to atmospheric heating over Tibetan Plateau in summer. *Clim. Dyn.* **2019**, *53*, 3419–3429. [CrossRef]
53. Liu, Y.M.; Wang, Z.Q.; Zhuo, H.F.; Wu, G.X. Two types of summertime heating over Asian large-scale orography and excitation of potential-vorticity forcing II. Sensible heating over Tibetan-Iranian Plateau. *Sci. China Earth Sci.* **2017**, *60*, 733–744. [CrossRef]
54. Chou, M.D.; Wu, C.H.; Kau, W.S. Large-Scale Control of Summer Precipitation in Taiwan. *J. Clim.* **2011**, *24*, 5081–5093. [CrossRef]
55. Wei, W.; Zhang, R.H.; Wen, M.; Rong, X.Y.; Li, T. Impact of Indian summer monsoon on the South Asian High and its influence on summer rainfall over China. *Clim. Dyn.* **2014**, *43*, 1257–1269. [CrossRef]
56. Ning, L.; Liu, J.; Wang, B. How does the South Asian High influence extreme precipitation over eastern China? *J. Geophys. Res.-Atmos.* **2017**, *122*, 4281–4298. [CrossRef]
57. Zhang, S.B.; Meng, L.X.; Zhao, Y.; Yang, X.Y.; Huang, A.N. The Influence of the Tibetan Plateau Monsoon on Summer Precipitation in Central Asia. *Front. Earth Sci.* **2022**, *10*, 771104. [CrossRef]
58. Li, J.J.; Chen, J.H.; Lu, C.S.; Wu, X.Q. Impacts of TIPEX-III Rawinsondes on the Dynamics and Thermodynamics Over the Eastern Tibetan Plateau in the Boreal Summer. *J. Geophys. Res.-Atmos.* **2020**, *125*, e2020JD032635. [CrossRef]
59. Sivan, C.; Kottayil, A.; Legras, B.; Bucci, S.; Mohanakumar, K.; Satheesan, K. Tracing the convective sources of air at tropical tropopause during the active and break phases of Indian summer monsoon. *Clim. Dyn.* **2022**, *59*, 2717–2734. [CrossRef]
60. Winker, D.M.; Vaughan, M.A.; Omar, A.; Hu, Y.X.; Powell, K.A.; Liu, Z.Y.; Hunt, W.H.; Young, S.A. Overview of the CALIPSO Mission and CALIOP Data Processing Algorithms. *J. Atmos. Ocean. Technol.* **2009**, *26*, 2310–2323. [CrossRef]
61. Song, Q.Q.; Zhang, Z.B.; Yu, H.B.; Ginoux, P.; Shen, J. Global dust optical depth climatology derived from CALIOP and MODIS aerosol retrievals on decadal timescales: Regional and interannual variability. *Atmos. Chem. Phys.* **2021**, *21*, 13369–13395. [CrossRef]
62. Yu, H.B.; Yang, Y.; Wang, H.L.; Tan, Q.; Chin, M.; Levy, R.C.; Remer, L.A.; Smith, S.J.; Yuan, T.L.; Shi, Y.X. Interannual variability and trends of combustion aerosol and dust in major continental outflows revealed by MODIS retrievals and CAM5 simulations during 2003–2017. *Atmos. Chem. Phys.* **2020**, *20*, 139–161. [CrossRef] [PubMed]
63. Gelaro, R.; McCarty, W.; Suarez, M.J.; Todling, R.; Molod, A.; Takacs, L.; Randles, C.A.; Darmenov, A.; Bosilovich, M.G.; Reichle, R.; et al. The Modern-Era Retrospective Analysis for Research and Applications, Version 2 (MERRA-2). *J. Clim.* **2017**, *30*, 5419–5454. [CrossRef] [PubMed]
64. Yao, W.R.; Che, H.Z.; Gui, K.; Wang, Y.Q.; Zhang, X.Y. Can MERRA-2 Reanalysis Data Reproduce the Three-Dimensional Evolution Characteristics of a Typical Dust Process in East Asia? A Case Study of the Dust Event in May 2017. *Remote Sens.* **2020**, *12*, 902. [CrossRef]
65. Randles, C.A.; da Silva, A.M.; Buchard, V.; Colarco, P.R.; Darmenov, A.; Govindaraju, R.; Smirnov, A.; Holben, B.; Ferrare, R.; Hair, J.; et al. The MERRA-2 Aerosol Reanalysis, 1980 Onward. Part I: System Description and Data Assimilation Evaluation. *J. Clim.* **2017**, *30*, 6823–6850. [CrossRef]
66. Buchard, V.; Randles, C.A.; da Silva, A.M.; Darmenov, A.; Colarco, P.R.; Govindaraju, R.; Ferrare, R.; Hair, J.; Beyersdorf, A.J.; Ziemba, L.D.; et al. The MERRA-2 Aerosol Reanalysis, 1980 Onward. Part II: Evaluation and Case Studies. *J. Clim.* **2017**, *30*, 6851–6872. [CrossRef]
67. Kanamitsu, M.; Ebisuzaki, W.; Woollen, J.; Yang, S.K.; Hnilo, J.J.; Fiorino, M.; Potter, G.L. NCEP-DOE AMIP-II reanalysis (R-2). *Bull. Am. Meteorol. Soc.* **2002**, *83*, 1631–1643. [CrossRef]
68. Nan, Y.; Wang, Y.X. De-coupling interannual variations of vertical dust extinction over the Taklimakan Desert during 2007–2016 using CALIOP. *Sci. Total Environ.* **2018**, *633*, 608–617. [CrossRef] [PubMed]
69. Dong, Q.Q.; Huang, Z.W.; Li, W.R.; Li, Z.; Song, X.D.; Liu, W.T.; Wang, T.H.; Bi, J.R.; Shi, J.S. Polarization Lidar Measurements of Dust Optical Properties at the Junction of the Taklimakan Desert-Tibetan Plateau. *Remote Sens.* **2022**, *14*, 558. [CrossRef]
70. Wang, T.H.; Chen, Y.X.; Gan, Z.W.; Han, Y.; Li, J.M.; Huang, J.P. Assessment of dominating aerosol properties and their long-term trend in the Pan-Third Pole region: A study with 10-year multi-sensor measurements. *Atmos. Environ.* **2020**, *239*, 117738. [CrossRef]
71. Liu, Y.; Liu, R.G. Climatology of dust storms in northern China and Mongolia: Results from MODIS observations during 2000–2010. *J. Geogr. Sci.* **2015**, *25*, 1298–1306. [CrossRef]
72. Liu, C.; Zhao, T.L.; Yang, X.H.; Liu, F.; Han, Y.X.; Luan, Z.P.; He, Q.; Rood, M.; Yuen, W.K. Observational study of formation mechanism, vertical structure, and dust emission of dust devils over the Taklimakan Desert, China. *J. Geophys. Res.-Atmos.* **2016**, *121*, 3608–3618. [CrossRef]

73. Yang, X.H.; Shen, S.H.; Yang, F.; He, Q.; Ali, M.; Huo, W.; Liu, X.C. Spatial and temporal variations of blowing dust events in the Taklimakan Desert. *Theor. Appl. Climatol.* **2016**, *125*, 669–677. [CrossRef]
74. Wei, W.; Zhang, R.H.; Yang, S.; Li, W.H.; Wen, M. Quasi-Biweekly Oscillation of the South Asian High and Its Role in Connecting the Indian and East Asian Summer Rainfalls. *Geophys. Res. Lett.* **2019**, *46*, 14742–14750. [CrossRef]
75. Banerjee, P.; Satheesh, S.K.; Moorthy, K.K. The Unusual Severe Dust Storm of May 2018 Over Northern India: Genesis, Propagation, and Associated Conditions. *J. Geophys. Res.-Atmos.* **2021**, *126*, e2020JD032369. [CrossRef]